



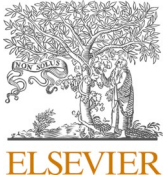
Intergranular oxidation of additively manufactured Ni-base alloy 625: The role of Si

Downloaded from: <https://research.chalmers.se>, 2024-03-08 14:45 UTC

Citation for the original published paper (version of record):

Chyrkin, A., Nowak, W., Gündüz, K. et al (2023). Intergranular oxidation of additively manufactured Ni-base alloy 625: The role of Si. *Corrosion Science*, 219.
<http://dx.doi.org/10.1016/j.corsci.2023.111234>

N.B. When citing this work, cite the original published paper.



Intergranular oxidation of additively manufactured Ni-base alloy 625: The role of Si

A. Chyrkin^{a,*}, W.J. Nowak^b, K.O. Gunduz^{a,c}, I. Fedorova^{d,1}, M. Sattari^d, J. Froitzheim^a, M. Halvarsson^d, K.M. Stiller^d

^a Chalmers University of Technology, Department of Chemistry and Chemical Engineering, Kemivägen 10, 41296 Gothenburg, Sweden

^b Rzeszow University of Technology, Faculty of Mechanical Engineering and Aeronautics, Department of Materials Science, al., Powstanców Warszawy 12, 35959 Rzeszow, Poland

^c Gebze Technical University, Department of Materials Science and Engineering, Gebze, 41400 Kocaeli, Turkey

^d Chalmers University of Technology, Department of Physics, Kemigården 1, 41296 Gothenburg, Sweden



ARTICLE INFO

Keywords:

Ni-base alloys
Alloy 625
Additive manufacturing
High-temperature corrosion
Oxidation
Intergranular oxidation

ABSTRACT

Additively manufactured (AM) Ni-base alloy 625 exposed in air and H₂/H₂O at 900 °C has been shown to suffer from intergranular oxidation attack unlike its conventionally manufactured (CM) variant. Modification of the AM microstructure via hot-rolling and heat-treatment did not alter the oxidation pattern. Detailed analysis of minor differences in chemical composition of AM and CM exposed the critical role of Si in oxidation protection of alloy 625. Experiments with model alloys as well as diffusion modeling confirmed the crucial role of a minimum Si concentration to form a SiO₂ subscale preventing thereby intergranular oxidation attack.

1. Introduction

Additive manufacturing (AM) of Ni-base superalloys has been attracting more and more attention especially in the aero-engine technology where AM of complex shaped components offers significant advantages [1–4].

Due to their outstanding mechanical and oxidation properties, alloys 718 and 625 are widely used and well-studied among the commercially available Ni-base superalloys in AM with respect to oxidation resistance [5–14].

One important aspect of AM is the formation of specific microstructures with anisotropic properties for parallel and perpendicular directions with respect to the building direction, which is shown to affect mechanical properties [15–17] but not the oxidation rate [6,10]. Yet, it is possible to obtain equiaxed grains with isotropic properties by adjusting the printing parameters and/or performing heat-treatment after the printing process [12,13,18,19–21].

As AM of Ni-base superalloys is still an emerging technology, the mechanical properties of these as-built alloys are commonly inferior to those of the CM counterparts due to pore and crack formation, lack of fusion between powder particles, Laves- and δ-phase formation due to

fast melting and solidification cycles [22–25]. To heal the AM-induced defects, hot isostatic pressing (HIP) can be employed as a post processing strategy coupled with heat-treatments to homogenize the microstructure and improve the mechanical properties [26–28]. However, a recent study by Sanchez et al. showed that alloy 718 produced by PBF-LB provided equal creep rates with 24% more creep lifetime compared to its wrought CM version when built by means of a Meander build strategy and heat-treated without the application of HIP [29]. Similar improvements for alloy 625 alloy were achieved by optimizing printing parameters as well as heat-treatment by Nguejio et al. [30].

In addition to mechanical properties, high-temperature oxidation resistance of AM Ni-base alloys is also a crucial factor to make the AM components functional and competitive. A limited number of comprehensive studies are available in the literature [5–8,31,32] on the oxidation properties of AM Ni-base alloys, including alloy 625 [9–14, 33]. Up to date, the main consensus points in these studies are: I) Oxidation rates are higher for AM Ni-base superalloys compared to their CM counterparts; II) Anisotropy has virtually no effect on the oxidation kinetics; III) In contrast to CM, additive manufactured alloys 718 and 625 may suffer from severe intergranular oxidation.

Although the afore-mentioned studies give a relatively conclusive

* Corresponding author.

E-mail address: chyrkin@chalmers.se (A. Chyrkin).

¹ Formerly with Chalmers University of Technology, Currently at Kanthal AB, Sörkvärnsvägen 3, 734 27 Hallstahammar, Sweden.

Table 1

Overview of materials and heat treatments used in this study.

Abbreviation	Metallurgical state	Grain size [μm]
AM	PBF-LB manufactured alloy 625 in the as-built condition.	13–42
AM-Y	Y-cut of AM parallel to build axis in the as-built condition	13
AM-Z	Z-cut of AM perpendicular to build axis in the as-built condition	42
AM-HT1	AM after heat-treatment for 24 h at 1200 °C	61
AM-HT2	AM after heat-treatment for 200 h at 1100 °C	48
AM-HR	AM after hot rolling at 980 °C	15
AM-CG	AM after annealing for 100 h at 1250 °C to obtain a coarse-grained structure	2500
CM	Conventional hot-forged alloy 625	10
MA	Model alloy NiCrNbMo, hot-rolled at 980 °C	28
MA-Si	Model alloy NiCrNbMoSi, hot-rolled at 980 °C	37

empirical picture of the oxidation behavior, they do not provide a clear and unanimous answer to the key questions:

- Why does this severe intergranular oxidation occur in AM but not CM?
- Is this difference in oxidation behavior due to specific microstructures in AM materials or rather minor differences in chemical composition between AM and CM alloys?

In our previous publication [34], we demonstrated that intergranular oxidation of AM alloy 625 featured by a characteristic ridge-void (RV) oxide scale morphology does not originate from the specific AM microstructure or reaction conditions. The RV oxidation morphology was reproduced in the AM material after hot-rolling, various heat-treatments, at different exposure temperatures, as well as in different gases. Only the hot-forged variant of CM alloy 625 revealed no intergranular oxidation, as reported in numerous previous studies [10, 35–38]. Based on the abundant experimental evidence, it was concluded that such a difference in oxidation behavior between AM and CM most probably originated from the variations in alloy chemical composition within the specification [34]. The goal of the present follow-up study was to establish a direct relationship between the chemical composition of the AM and CM variants and their oxidation behavior, i.e., to determine the alloying element(s) responsible for intergranular oxidation attack.

2. Experimental

2.1. Materials

Cubes of as-built AM alloy 625 with the dimensions of 15×15×15 mm³ were additively manufactured using Powder Bed Fusion – Laser Beam (PBF-LB) by Siemens Energy AB (Finspång, Sweden). The alloy specimens were sectioned in 2 directions: parallel (625 AM-X and 625 AM-Y) and perpendicular (625 AM-Z) to the build axis. Since the microstructures of X-cut and Y-cut are identical [34], only AM Y-cut is

reported in this study. Heat-treatments of AM alloy 625 to remove the AM microstructure and obtain bigger grains were carried out at 1100 and 1250 °C in vacuum (10⁻⁵ mbar). The sectioned alloy coupons were sealed in evacuated quartz capsules and annealed for 200 h at 1100 °C and 100 h at 1250 °C, respectively. The annealed specimens were quenched in water. These specimens are termed AM-HT (200 h, 1100 °C) and AM-CG (100 h at 1250 °C).

To modify the typical AM structure, one as-built AM alloy 625 cube was hot-rolled by HMW Hauner GmbH (Röttenbach, Germany). After heating to 980 °C the ingot was rolled to 2.5 mm thick sheet, held for 2 h at 1000 °C and quenched in water. A homogeneous microstructure containing equiaxed grains with the average grain size of 15 μm was thus obtained.

As a reference material, the CM alloy 625 specimens were machined from a hot-forged bar supplied by Huntington Alloy Corp. The batch specific composition can be found in ref [35]. Additionally, two model alloys NiCrMoNb (designated MA) and NiCrMoNbSi (designated MA-Si) were produced by HMW Hauner GmbH (Röttenbach, Germany) to investigate the effect of Si on the intergranular oxidation of alloy 625. The two model alloys were arc-melted in vacuum from 99.99% pure metals, hot-rolled at 1000 °C to a 2 mm thick sheet, held for 2 h at 1000 °C and quenched in water. All materials as well as microstructural modifications tested in the present study are summarized in Table 1.

The chemical compositions of the alloys prior to exposures were determined using Glow Discharge-Optical Emission Spectroscopy (GD-OES) and are given in Table 2, the functional role of the alloying elements being highlighted. Prior to exposures, the alloy coupons of all studied alloys were machined to the 15×15×2 or 20×10×2 mm³ dimensions. The surfaces were ground with SiC papers and polished down to 0.25 μm with diamond pastes.

2.2. Exposures

Isothermal exposures were performed in tube furnaces at 900 °C for up to 300 h in laboratory air with ambient humidity. The specimens, degreased in ethanol and acetone prior to exposure, were directly introduced into the hot zone of the tube furnace. Temperature control was assured by an external Pt/Rh-thermocouple placed next to the specimens. After exposures, the specimens were rapidly removed from the hot zone and cooled down in air.

To check the influence of the chromia scaling mechanism, i.e., oxide growth direction, on intergranular corrosion, the exposures in a flow of Ar-5 H₂–3%H₂O were performed in a closed, gas-tight quartz tube. It is well known that water vapor promotes inward growth of Cr₂O₃ and this inwardly grown chromia usually grows faster and adheres better to metal [35,39,40]. The Ar-5%H₂ gas mixture supplied by Linde gas (AGA AB, Lidingö, Sweden) was bubbled through a humidification setup held at 24.4 °C to obtain 3% absolute humidity (30 mbar of H₂O). Unlike the air exposures, the specimens were introduced into a cold furnace, flushed with the gas mixture for 1 h, heated at 10 °C/min to reach 900 °C and exposed under 250 ml/min flow rate. The cooling rate was 10 °C/min as well.

Table 2Chemical composition of studied alloys determined by GD-OES^a [wt%].

Functionality of alloying elements	base/oxidation		strengthening		neutral	external scale		internal oxidation		carbide
	Alloy	Ni	Cr	Mo	Nb	Fe	Mn	Ti	Al	Si
CM 625 **	Bal.	21.6	8.9	3.5	3.6	0.11	0.33	0.32	0.27	0.02
AM GD-OES	Bal.	20.7	9.7	4.0	0.8	0.05	0.36	0.29	0.08	0.01
MA	Bal.	21.5	9.6	4.0	-	-	-	-	-	-
MA-Si	Bal.	21.7	9.4	4.1	-	-	-	-	0.32	-

^{**}Composition of CM alloy 625 from reference [35]^a Detection limit for GD-OES is at least 100 wppm or 0.01 wt%

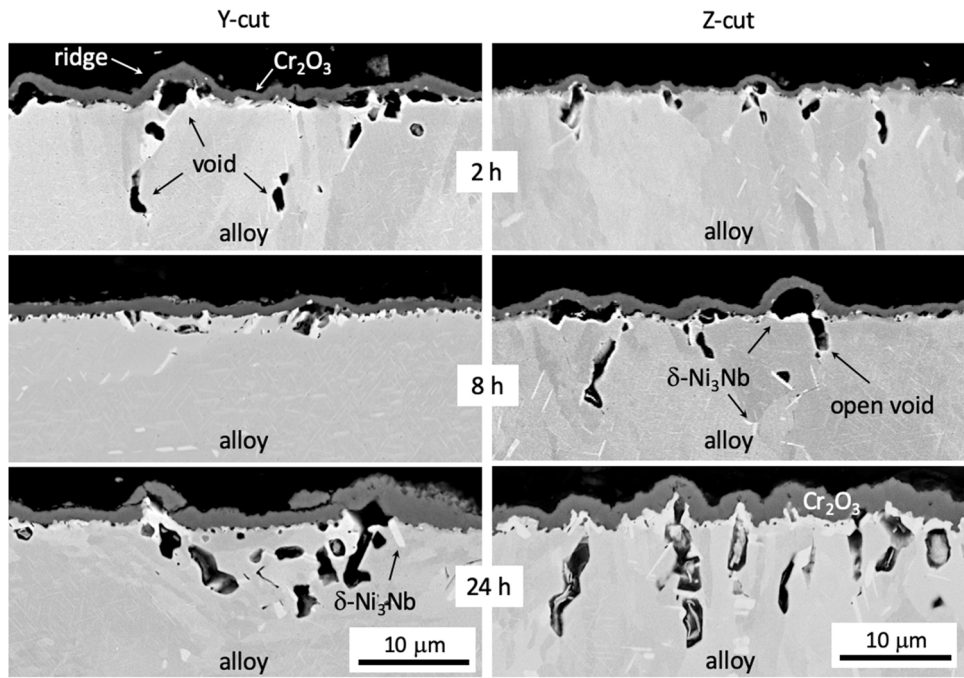
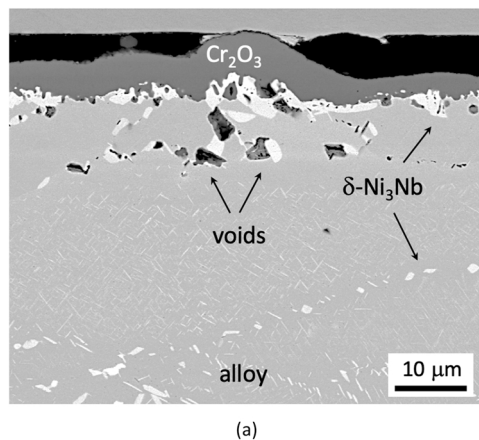
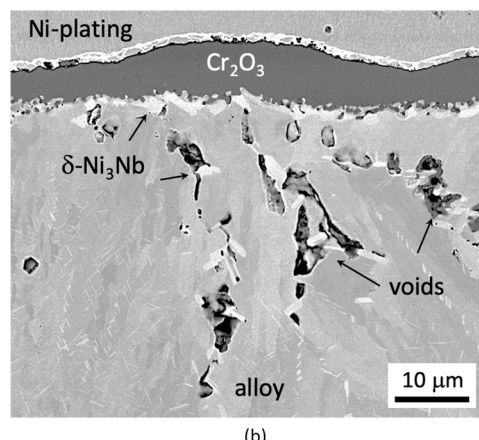


Fig. 1. Temporal evolution of oxide scale morphology on AM alloy 625 during early stages of air oxidation at 900 °C.



(a)



(b)

Fig. 2. BSE images of oxide scales grown on AM alloy 625 after 168 h exposure in Ar-5%H₂-3%H₂O at 900 °C: (a) Y-cut, (b) Z-cut.

2.3. Microstructural characterization

An FEI Quanta 200 ESEM (environmental scanning electron microscope) equipped with an energy dispersive X-ray spectrometer (EDS) was employed for microstructural analyses. Cross-sections were made from exposed samples by conventional polishing with diamond pastes and colloidal silica after hot mounting or by the broad-ion beam (BIB) technique using a Leica EM TIC 3X. The air exposed specimens demonstrated poor oxide adherence and had to be electroplated with nickel after gold sputtering to prevent oxide exfoliation during sample preparation. GD-OES spectra, as well as concentration profiles, were obtained using a Horiba Jobin Yvon spectrometer. The GD-OES depth profiles were quantified following the procedure described in [41–43].

3. Results

A temporal evolution of the oxide scale on AM alloy 625 during early stages of air oxidation at 900 °C is presented in the backscattered electron (BSE) images in Fig. 1. A characteristic RV oxide scale morphology described in detail in our previous study [34] can be observed at the very early stages of oxidation. The external chromia buckles by the growth stress and delaminates specifically over the grain boundaries. Oxide buckling opens up the underlying voids at the grain boundaries (GB) thereby promoting intergranular oxidation attack. An identical oxidation morphology was reported for AM alloy 625 in [13,33].

BSE images of cross-sectioned AM alloy 625 specimens for both Y- and Z cuts after 168 h exposure in Ar-5%H₂-3%H₂O at 900 °C are displayed in Fig. 2. The chromia scales grown in a H₂-H₂O gas mixture are pore-free and much smoother compared to the air grown Cr₂O₃ scales (compare with Fig. 1). Being more uniform and homogeneous, the H₂-H₂O grown chromia scales additionally demonstrate a better adherence to the metal [40,44] and show no signs of delamination over GBs. However, smooth oxide bulges are visible over the GBs accompanied by abundant porosity in the alloy subsurface. The GB voids are aligned along the GBs correlating thus with the structural anisotropy of the alloy and the cutting direction. The Z-cut samples have acicular elongated grains with a higher GB density. Therefore, Z-cut samples revealed a deeper GB porosity.

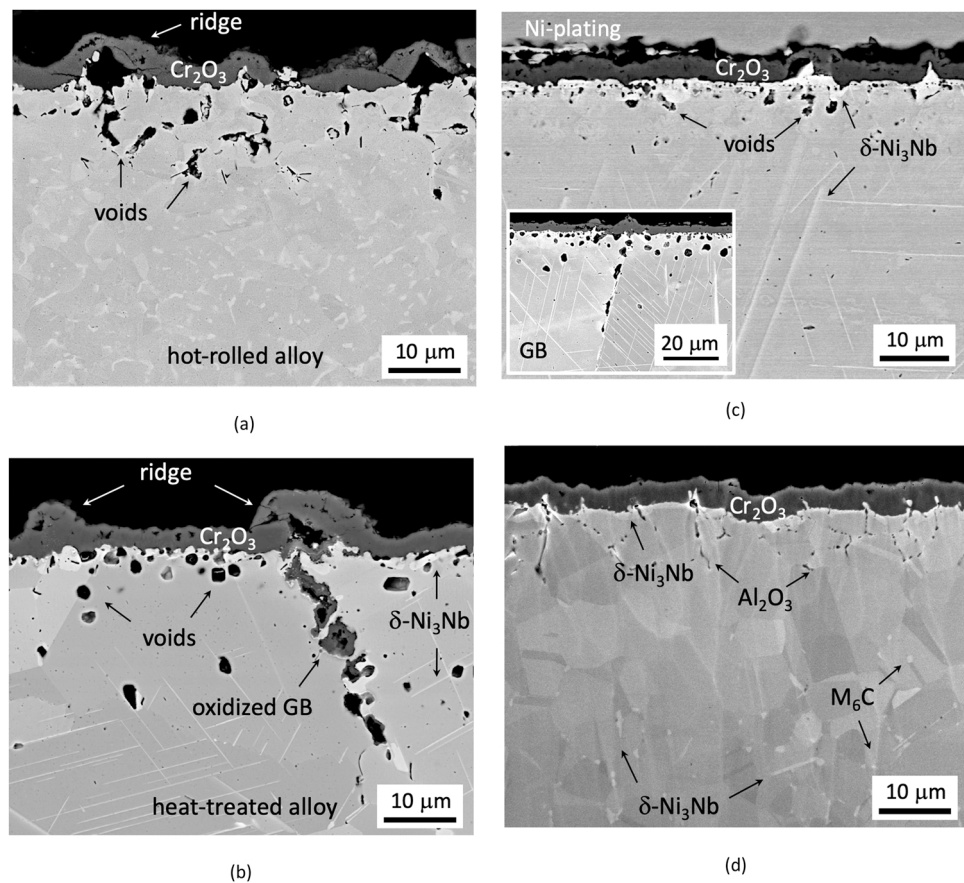


Fig. 3. Effect of microstructure on oxide scale morphology after 168 h of air oxidation at 900 °C: (a) after hot rolling, (b) after 200 h heat-treatment at 1100 °C, (c) after grain coarsening for 72 h at 1250 °C, (d) conventionally manufactured (CM) alloy 625.

Fig. 3 illustrates the effect of microstructure, specifically the grain size, on the oxide scale morphology of AM alloy 625 [34]. Irrespective of the grain size obtained either by hot-rolling (**Fig. 3a**) or various heat-treatments (**Fig. 3b, c**), all AM alloy 625 variants revealed the typical RV morphology of the oxide scale at the GBs. Only the hot-forged CM alloy 625 (**Fig. 3d**) showed absolutely no sign of RV associates.

Fig. 4 demonstrates EDS elemental maps for the cross-sectioned AM-Y, AM-Z and CM specimens after 300 h air oxidation 900 °C. The elements in the maps are grouped according to their primary role in the metallurgical design of alloy 625 and their involvement in the oxidation pattern: external oxide scale (Cr, O, Ti), precipitation and solution strengthening (Nb and Mo) and internal oxidation (Al and Si). The EDS maps in **Fig. 4** reproduce all oxidation-induced compositional and microstructural changes previously reported for alloy 625 in literature [35,37,45], i.e., i) incorporation of Ti into the outer Cr₂O₃ scale, ii) enrichment/depletion of Nb and Mo in the immediate vicinity of the outer oxide scale, iii) internal oxidation of Al and Si. Note the formation of SiO₂ beneath the Cr₂O₃ scale in CM.

The oxidation kinetics of model alloys MA and MA-Si exposed in air and Ar-5%H₂-3%H₂O at 900 °C for up to 300 h are compared in **Fig. 5**. The weigh change data for as-built AM alloy 625 and CM alloy 625 are also given in **Fig. 5** as a reference for both MA and MA-Si. In air, the Si-free model alloy MA oxidized at the same rate as the AM alloy 625. It is noteworthy that the oxidation rate of AM alloy 625 in air is independent of the alloy texture as demonstrated [10,12,33,34]. The model alloy MA-Si showed lower oxidation kinetics comparable with that of CM alloy 625 along with a higher tendency for oxide spallation (**Fig. 5a**). To overcome this problem and obtain comparable oxidation kinetics data, an additional exposure in Ar-5%H₂-3%H₂O was undertaken. Indeed, the exposure in a H₂-H₂O gas resulted in much better adherent oxide scales

and no oxide spallation (**Fig. 5b**). The oxidation rates for both MA and MA-Si were lower than those for AM alloy 625 and even CM alloy 625 in Ar-5%H₂-3%H₂O. In both atmospheres, addition of Si resulted in a lower oxidation rate.

Fig. 6 shows GD-OES concentration profiles in the oxidation affected zones in various AM (as-built, hot-rolled and heat-treated) and CM specimens after 168 h of air oxidation at 900 °C. A number of clear differences in the depletion zones can be distinguished between all variants of AM and CM, which is related to the different alloy microstructures. In all profiles in **Fig. 6**, the following features for the alloy 625 subsurface depletion pattern can be stated: i) Cr-depletion towards the oxide-metal interface, ii) Nb-enrichment immediately underneath the Cr₂O₃ scale (see the subscale δ-phase enrichment in **Figs. 1–3**), iii) slight enrichment of “inert” Mo and Fe, iv) internal oxidation of Al and Si (note also internal oxidation in **Fig. 3c,d**), v) outward diffusion of Ti and Mn and their incorporation into the chromia scale accompanied by depletion in the underlying alloy and vi) back diffusion of carbon [35].

Although the depth profiles in AM-Z and AM-Y are qualitatively very similar (**Fig. 6a,b**), the oxidation-affected zone marked by a kink of the Nb and Mo profiles in AM-Z is deeper (70 μm) compared to that in AM-Y (50 μm). This zone shrunk to 30 μm in a hot-rolled AM and 25 μm in a coarsened AM which virtually simulated a single-crystal. The latter values are close to that in CM alloy 625 (30 μm). Elongated columnar grains in AM-Z are the most plausible reason of a deeper depletion in the as-built AM specimens.

Another remarkable feature of the GD-OES profiles separately highlighted in **Fig. 7** are the internally oxidizing elements, i.e., silicon and aluminum. The Al profiles (**Fig. 7a**) demonstrated a strong microstructural dependence mentioned above as Al₂O₃ specifically tends to precipitate at GBs (**Fig. 3d**). Therefore, the deepest IOZ (internal

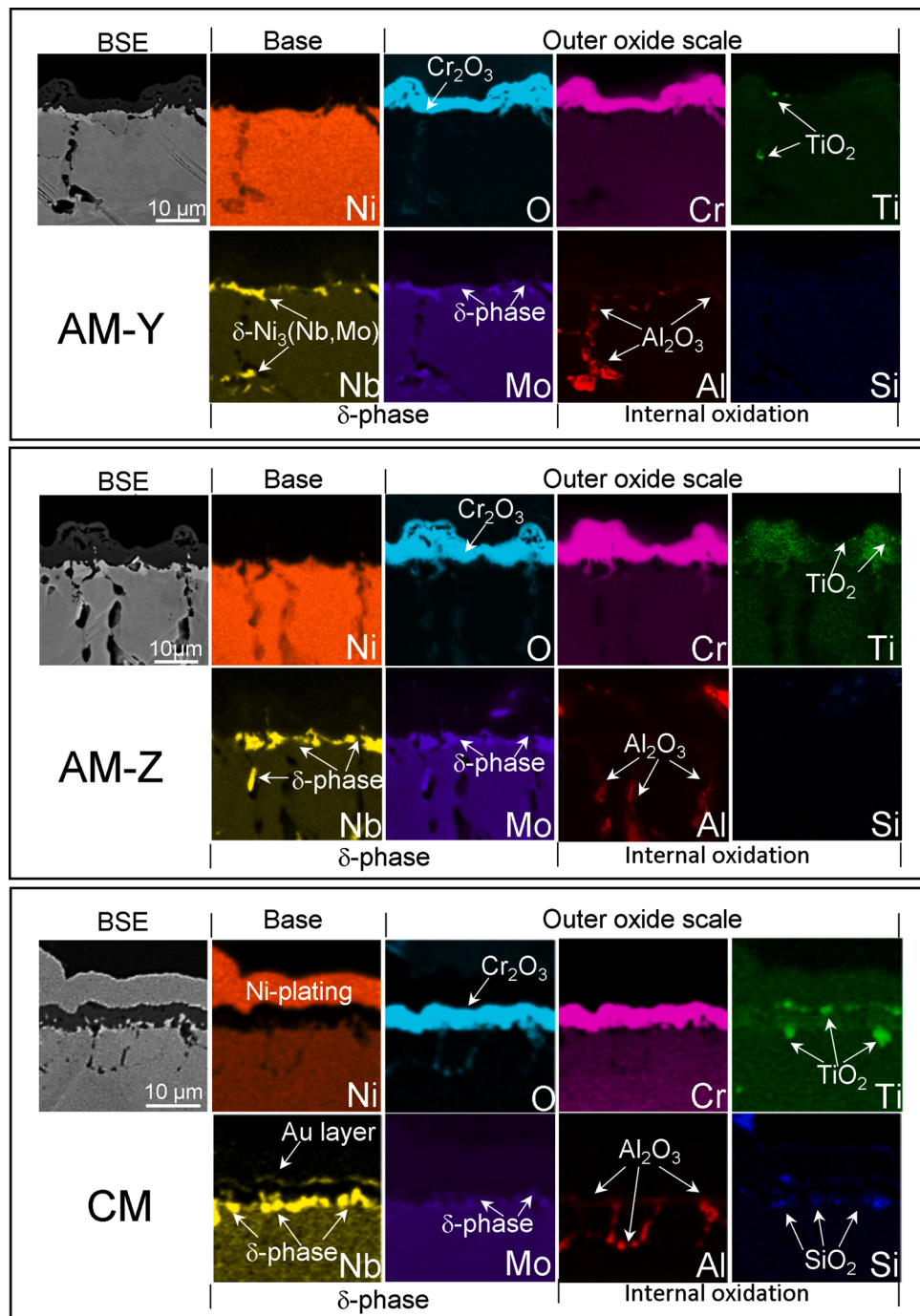


Fig. 4. EDS elemental map of the oxide scale for AM-Y, AM-Z and CM alloy 625 after 300 h air oxidation at 900 °C.

oxidation zone) was detected in AM-Z, while the thinnest ones were found in CM and AM-HT. As was demonstrated in [34], Al preferentially oxidized in the GB voids in the AM material, while only decorating GBs with small precipitates in CM. Interestingly, internal alumina in AM-CG homogenized at 1250 °C is uniformly distributed in the alloy subsurface (Fig. 3c) and precipitated at the oxide-alloy interface (note the peak for AM-CG in Fig. 7a). Unlike aluminum, the Si depth profiles (Fig. 7b) in all AM variants are rather uniform suggesting no involvement of the GBs in precipitation of SiO₂. The biggest difference between AM and CM was a distinct Si peak observed in the latter (see also Si map in Fig. 4). A similar peak was recorded in the Si alloyed model alloy MA-Si. Finally, CM was found to contain more Si than the AM variants (see also Table 2).

Fig. 8 shows the oxide scales grown on model alloys MA and MA-Si during early stages of air oxidation at 900 °C. Similar to AM alloy 625, a Si-free variant MA formed a characteristic RV oxide scale morphology: a buckled oxide accompanied by elongated GB voids which tend to oxidize as the exposure proceeds. Addition of 0.3 wt% Si to the model alloy MA (Table 2) resulted in three microstructural effects: i) a thinner oxide scale, ii) elimination of oxide ridges, iii) disappearance of GB voids. In parallel, Si impaired oxide adherence leading to intense oxide spallation (Fig. 5a).

A separate exposure in Ar-5%H₂-3%H₂O allowed to maintain the chromia scale after longer exposure times (Fig. 5b) and resulted in very similar oxide morphologies displayed in Fig. 9. The Si-free model alloy formed GB voids which disappeared after alloying with Si.

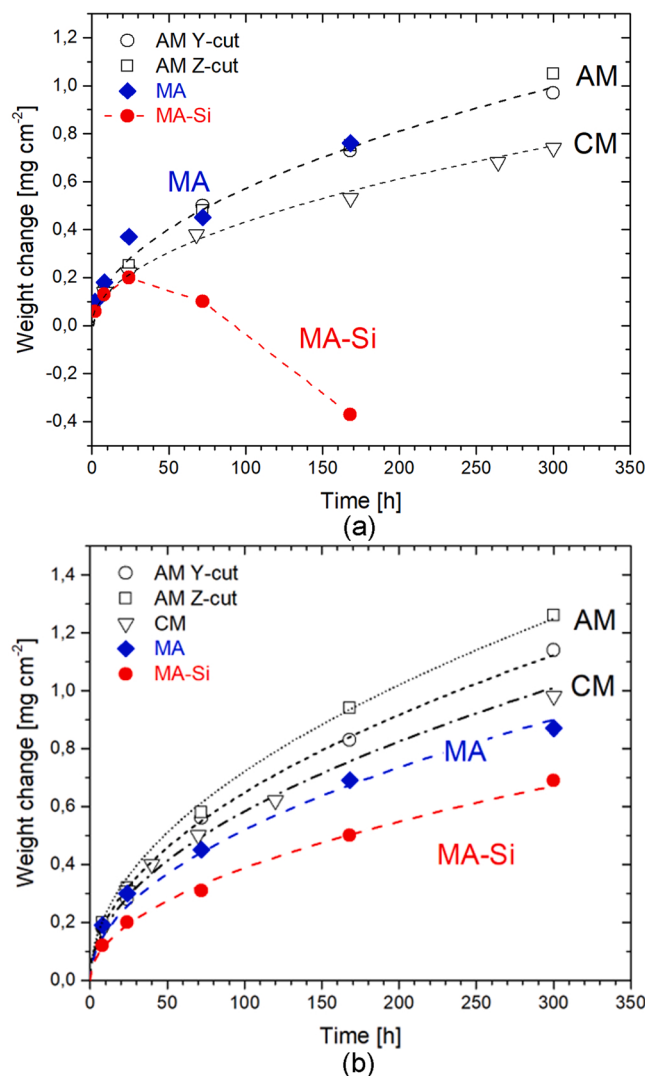


Fig. 5. Oxidation kinetics of AM alloy 625, CM alloy 625 and model alloys MA and MA-Si during oxidation in (a) air and (b) Ar-5%H₂-3%H₂O at 900 °C.

4. Discussion

4.1. Effect of grain size

Additively manufactured Ni-base alloys are known to suffer from intergranular oxidation attack at 900–1000 °C [7,8,10,31] which is the main reason for higher oxidation rates reported for AM alloys compared to their CM counterparts. Intergranular oxidation often occurs in the GB voids formed underneath oxide ridges (Figs. 1–3). Parizia et al. [13] reported oxide buckling as well as elongated voids at alloy GBs forming after 96 h air oxidation of additively manufactured alloy 625 at 900 °C. The same oxidation morphology was reported for air exposed AM alloy 625 at 900–1000 °C [33]. Ramenat et al. [10] observed only moderate oxidation of subsurface voids in AM alloy 625 at 1050 °C while no extensive void formation was detected at 900 °C. More commonly, intergranular oxidation was reported for AM alloy 718 fabricated by PBF-LB [6,46] and EBM (electron beam melting) [7,8] and sometimes even for wrought alloy 718 [8]. Indeed, the intergranular oxidation morphology was observed in AM alloy 625 tested in the present study and reproduced in a hot-rolled model alloy MA containing only the main constituents of alloys 625 and 718 (Fig. 8a).

Such systematic differences in oxidation behavior between AM and CM alloys can hardly be interpreted as just a batch-to-batch variation.

Three main sources of this variation can be inferred: i) specific AM microstructure; ii) minor differences in alloy/powder chemical composition; iii) AM process. The latter seems the least relevant as intergranular oxidation is independently reported for numerous AM alloys manufactured via different production routes. The AM microstructure of alloy 625 studied in the present investigation has no effect on the occurrence of intergranular oxidation attack. The characteristic RV morphology of the oxide scale appears at the earliest instants of oxidation (Fig. 1) and prevails irrespective of the actual alloy microstructure as long as the alloy chemical composition was maintained (Fig. 3). In other words, neither hot-rolling (Fig. 3a) nor grain coarsening via heat-treatment at 1100 °C (Fig. 3b) eliminated intergranular oxidation.

The modification of grain size affected the subsurface porosity pattern, but not the oxide scale morphology, i.e., the oxide ridges above GBs were associated with the GB voids prone to oxidation. At the same time, a profound homogenization at 1250 °C resulting in very large grains [47], mms in size, dramatically reduced the occurrence of ridge-void associates (Fig. 3c) and lowered the oxidation rate [34]. However, the remnant grain boundaries in the heat-treated AM specimens (inset in Fig. 3c) revealed the typical RV associate. Thus, the homogenization experiment unequivocally demonstrated the relationship between the occurrence of RV morphology and GB density.

While the RV morphology of the external chromia scale showed only a limited susceptibility to the alloy grain size (Figs. 1–3), internal oxidation of Si and Al demonstrated significantly different patterns in all modifications of AM alloy 625 and especially in comparison with CM alloy 625 (Fig. 7). The GD-OES profiles of Al (Fig. 7a) and Si (Fig. 7b) revealed totally different patterns of subsurface enrichment-depletion due to internal oxidation.

The Al-depletion profiles in Fig. 7a demonstrate a clear correlation between the depletion depth and the texture of the grains in AM alloy 625 alloy, e.g., the deepest penetration for AM-Z and the shallowest one for the variant AM-CG, virtually a single-crystal. In the latter, internal precipitates of both Al₂O₃ and SiO₂ are uniformly distributed in the alloy matrix (see Fig. 3c).

The Si-depletion profiles in Fig. 7b deserve special attention. First, the GD-OES profiles reveal a generally lower level of alloying of AM alloy 625 with Si compared to CM (see also Table 2). Second, unlike aluminum, the shape of the Si-profile is very similar for all AM alloy 625 variants indicating thus no involvement of GBs in the internal precipitation of SiO₂. Third and most important, a distinct peak of Si immediately underneath the outer Cr₂O₃ scale was measured in CM alloy 625 (see also Si map for CM in Fig. 4) while no such segregation of Si was found for AM, presumably due to a lower Si concentration in AM. In MA-Si a distinct peak of Si and a corresponding depletion zone can be found too.

As the alloy microstructure of AM alloy 625 is shown to have no effect on either the RV chromia scale morphology or the internal oxidation pattern of Si, the lower concentration of the latter in AM compared to CM, i.e., the alloy chemical composition not the microstructure, appears to be the key to understanding the mechanism of intergranular oxidation of the studied AM alloy 625 and maybe other AM high-temperature alloys [7,8,10,31].

4.2. Effect of minor alloying elements

The alloying elements in alloy 625 can be subdivided in several groups according to the metallurgical functionality and their role in oxidation (see also Table 2 and Fig. 4): i) oxidation/corrosion resistance – Cr; ii) strengthening – Mo (solution hardening) and Nb (precipitation hardening); iii) “neutral” base-elements – Fe and Co; iv) elements entering the Cr₂O₃ scale – Ti and Mn; v) internally oxidizing elements – Si and Al; vi) interstitials – C.

With respect to the intergranular oxidation, the main alloy constituents should be considered beyond suspicion as the NiCrMoNb model alloy MA reproduced the characteristic RV oxide scale morphology as

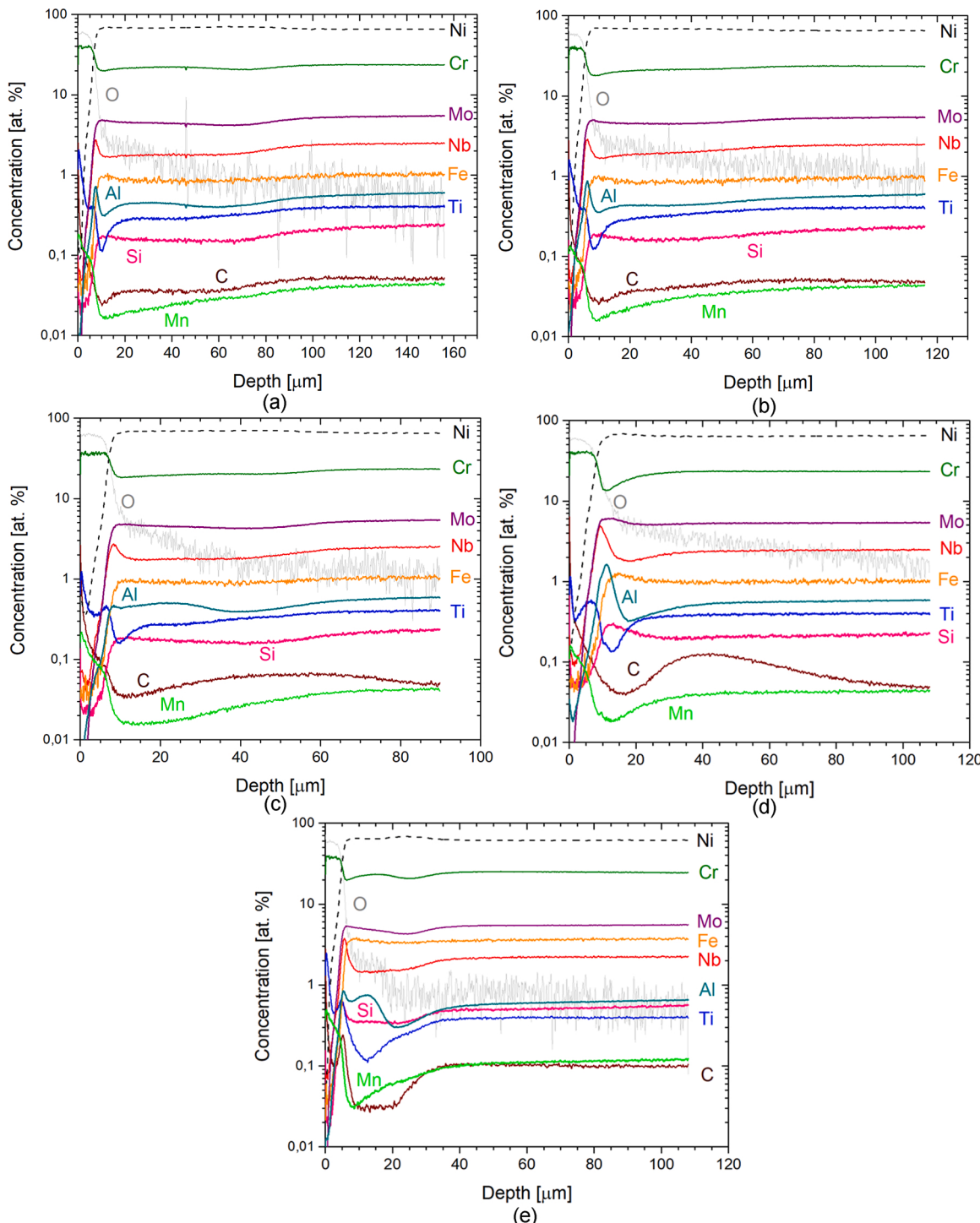


Fig. 6. GD-OES concentration profiles in alloy specimens air exposed for 168 h at 900 °C: (a) Z- and (b) Y-cut of as-built AM alloy 625, (c) AM after hot-rolling and (d) heat treatment at 1250 °C and (e) CM alloy 625 and.

well as the intergranular oxidation pattern (Fig. 8a). Despite the significant variation in Fe content between AM and CM (compare Fig. 6 a,b and e), iron can also be attributed to this group of main constituents as its impact on oxidation behavior of alloy 625 is very unlikely.

AM alloy 625 contains less carbon (0.01 wt%) than the CM batch (0.02 wt%), which is reflected in the as-received microstructure of AM material [34]: there is no M₆C carbide in the microstructure which is present in CM (Fig. 3d). The Ni₃Mo₃C carbide [48] is known to dissolve in the subsurface region of alloy 625 [35] although Cr is not its main constituent. The M₆C dissolution has been shown to be the consequence

of back diffusion of carbon induced by a Cr-depletion in the surface-near region [35,49–51]. Although carbon and other interstitial elements are known to affect diffusion in steels [52], pure nickel [53] and high-entropy alloys [54], it is very unlikely that carbon might be related to intergranular oxidation of AM alloy 625 as it migrates away from the surface during oxidation in both in AM and CM (Fig. 6).

Ti and Mn both enter the external Cr₂O₃ scale and demonstrate similar depletion profiles in CM as well as in AM irrespective of the microstructure (Fig. 6). It is well-known that titanium becomes incorporated in Cr₂O₃ during oxidation, dopes it and thereby increases the

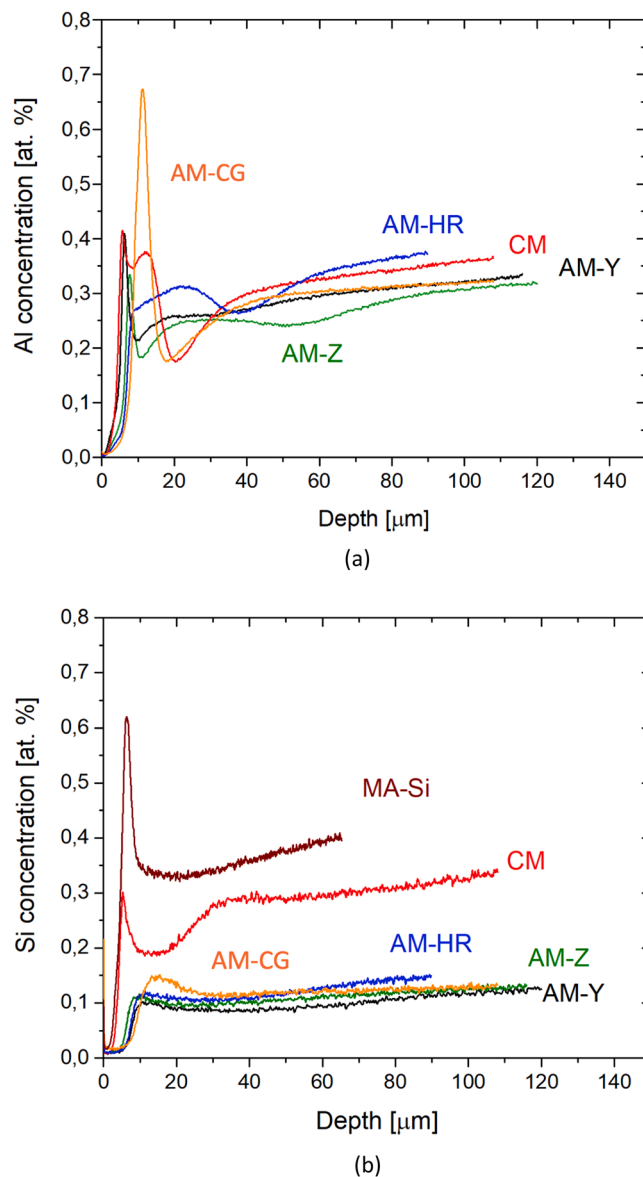


Fig. 7. GD-OES depth profiles of Al (a) and Si (b) in oxidized alloy specimens after 168 h exposure in air at 900 °C.

scaling rate [55–58]. In the present study, both CM and AM variants are alloyed to the same level with Ti (Table 2) and demonstrate identical thickness of the segments of the Cr₂O₃ scale over an entire grain between the GBs, e.g., 3.5 μm after 168 h air oxidation at 900 °C. Considering very similar shapes of the Ti-profiles in all alloy 625 variants (Fig. 6), titanium can hardly be expected to promote intergranular oxidation.

A similar logic can be applied to manganese. However, it should be noted that the Mn content of AM (0.05 wt%) is lower than that of CM (0.1 wt%, see Table 2). Mn is known to diffuse through the Cr₂O₃ and form an outer (Cr,Mn)₃O₄ top layer when typically alloyed with 0.3 wt% Mn [59–61].

This outer spinel layer [62] has been shown to significantly reduce reactive Cr-evaporation [59,63,64]. As in the case of Ti, very similar depletion-enrichment patterns of Mn in all AM variants as well as in CM alloy 625 (Fig. 6) suggest a low probability of its involvement in promoting intergranular oxidation in AM.

Finally, the internally oxidizing elements, such as Al and Si, demonstrated a strong dependence of the internal precipitation patterns, i.e., distribution at GBs, from the alloy microstructure (see previous section). The internal precipitates of Al₂O₃ tend to form perpendicular to

the interface [65,66] or at alloy GBs (Fig. 3d) whereas SiO₂ can form a continuous sublayer beneath the Cr₂O₃ scale (Si map for CM in Fig. 4 and Fig. 7b). The latter capacity of SiO₂ to serve as an additional diffusion barrier that limits Cr transport, especially the enhanced Cr flux emerging from the GB, resulting in a higher scaling rate over the GBs and oxide ridges, makes Si a better candidate for the “magical” element preventing intergranular oxidation in CM alloy 625. The dedicated experiments with model alloys simulating alloy 625 fully confirmed this hypothesis. Alloying with 0.3 wt% completely eliminated the RV morphology and intergranular oxidation attack (Fig. 8) which was reproduced in a Si-free model alloy MA and morphologically resembled very much that in all AM alloy 625 variants. The actual mechanism of oxidation protection by Si is further discussed in the following section.

4.3. Effect of silicon

The beneficial effect of Si on the oxidation behavior of chromia-forming high-temperature alloys has been known for a long time [67, 68]. Depending on the Si concentration and temperature, alloying with silicon promotes two basic scenarios: formation of a continuous SiO₂ subscale [69–71] or internal precipitation [68,72,73]. Even when the alloying level of Si is insufficient to produce a continuous SiO₂ layer, the beneficial effect of Si addition on the oxidation rate is evident [68,69,72, 73,74]. The following key mechanisms of the Si effect have been discussed in the literature: i) crystalline or amorphous silica is generally believed to serve as a diffusion barrier impeding the outward transport of Cr cations [70,72,73,75]; ii) Si enhances interdiffusion of Cr in Ni-Cr [75], which found a confirmation in thermodynamic modelling of the diffusion matrix in [65]; iii) SiO₂ precipitates provide additional nucleation sites for Cr₂O₃ [72] and suppress transient oxidation [76]. While decreasing the oxidation rate (Fig. 5), Si may have also an additional detrimental effect on the performance of a chromia-forming alloy promoting enhanced oxide spallation [69,74,75,77]. The adhesion of Cr₂O₃ deteriorates with increasing Si content above a certain level due to volume change of SiO₂ on cooling [78] or blocking influx of vacancies resulting in micro-cavities [74]. Nevertheless, the overall effect of moderate alloying with Si is rather positive and is widely practiced in the metallurgy of high-temperature alloys.

In the present study, all afore-mentioned effects of Si were observed: i) the oxidation rate of a Si-containing model alloy MA-Si decreased compared to the Si-free variant MA (Fig. 5a), ii) alloying with Si deteriorated the adhesion of Cr₂O₃, which was circumvented only via an exposure in Ar-5%H₂-3%H₂O, since chromia grown in H₂/H₂O atmosphere tends to grow predominantly inwards [39,40] and forms less-stressed, better adherent oxide scales [44]. In addition to these two well-studied effects, alloying the model alloy MA with 0.3 wt% Si had a dramatically positive effect on the oxide scale morphology (Fig. 9). Addition of Si simultaneously eliminated oxide buckling and ridge formation as well as intergranular oxidation attack. In the Ar-5%H₂-3%H₂O (Fig. 9b) the oxide scale does not buckle but still the formation of the voids at GBs is observed (Fig. 9a). Yet, addition of Si suppresses even the void formation in Ar-5%H₂-3%H₂O.

To better understand the impact of the Si content in AM alloy 625 (Fig. 7b) and its role in preventing intergranular oxidation in CM, the classical theories of internal and selective oxidation [79,80] must be employed to evaluate the ability of CM and AM to form a SiO₂ subscale, as demonstrated, e.g., in [81,82]. The formation and maintenance of a protective SiO₂ sublayer requires that two Wagnerian criteria are fulfilled. First, the Si concentration in the alloy must exceed a level, $N_{Si}^{(1)}$, necessary to overcome the oxygen ingress by outward Si preventing thereby internal precipitation:

$$N_{Si}^{(1)} > \left[\frac{\pi g^*}{2} \frac{V_m}{V_{SiO_2}} \frac{N_O^{(s)} D_O}{D_{Si}} \right]^{\frac{1}{2}} \quad (1)$$

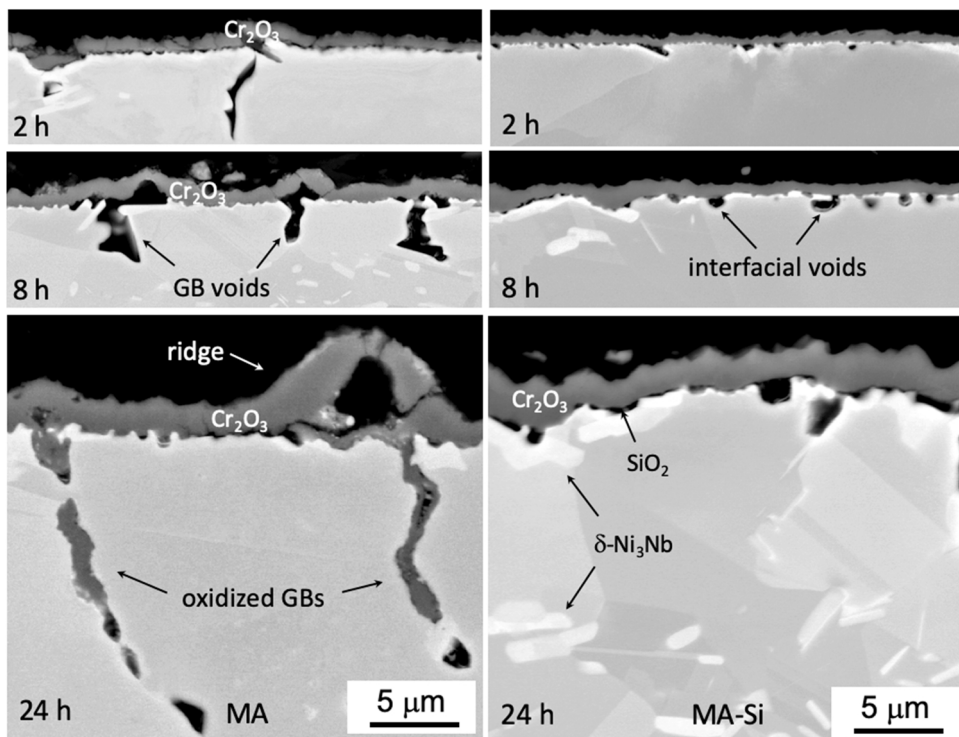


Fig. 8. Temporal evolution of oxide scale morphology on model alloys NiCrNbMo (MA) and NiCrNbMoSi (MA-Si) during early stages of air oxidation at 900 °C.

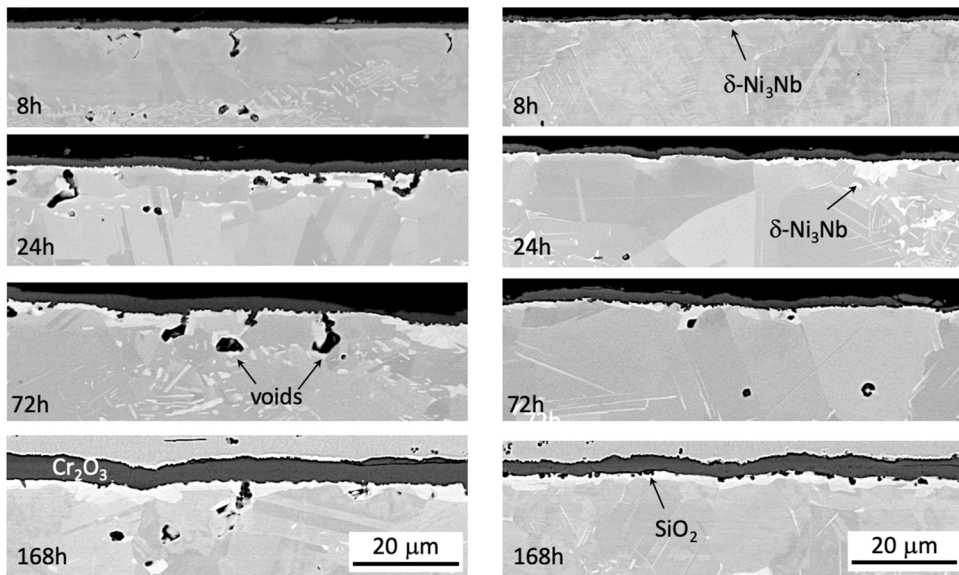


Fig. 9. Temporal evolution of oxide scale morphologies on model alloys NiCrNbMo (MA) and NiCrNbMoSi (MA-Si) during exposure in Ar-5%H₂-3%H₂O at 900 °C.

here $N_O^{(s)}$ is the oxygen solubility in the alloy in terms of mole-fraction, D_O is the diffusivity of oxygen in m^2s^{-1} , D_{Si} is the interdiffusion coefficient of Si in m^2s^{-1} , \bar{V}_m and \bar{V}_{SiO_2} are the molar volumes of the alloy and silica in $\text{m}^3\text{mole}^{-1}$, respectively. The factor g^* is the minimum volume-fraction of internal oxide needed to induce the transition from internal to external oxidation and was approximated as 0.3 by Rapp [83].

The second criterion was derived from Wagner's depletion model and predicts the minimum Si concentration in the alloy, $N_{Si}^{(2)}$, to sustain the scaling process once the SiO_2 layer is formed:

$$N_{Si}^{(2)} > \frac{\bar{V}_m}{\bar{V}_{SiO_2}} \left(\frac{\pi k_p}{2D_{Si}} \right)^{\frac{1}{2}} \quad (2)$$

here k_p is the parabolic rate constant for the SiO_2 sublayer in m^2s^{-1} .

The Si diffusion coefficient in nickel was obtained from [84]. As SiO_2 forms underneath the Cr_2O_3 scale, $N_O^{(s)}$ is governed by the $\text{Cr}/\text{Cr}_2\text{O}_3$ equilibrium at the oxide-alloy interface. The interfacial $p\text{O}_2$ was calculated to be 3.4×10^{-24} bar from the standard thermodynamic data [85], assuming ideal solution behavior of Cr in the alloy; $a_{Cr} = N_{Cr}$. The oxygen solubility and diffusivity were taken from [86]. The scaling rate of SiO_2 was difficult to determine from the available experimental data since

Table 3Critical silicon concentrations $N_{Si}^{(1)}$ and $N_{Si}^{(2)}$ at 900 °C.

\bar{V}_m [m ³ mol ⁻¹]	7.3×10^6
V_{SiO_2} [m ³ mol ⁻¹]	22.6×10^6
$N_O^{(S)}$	5.6×10^{-10}
D_O [m ² s ⁻¹]	2.4×10^{-13}
D_{Si} [m ² s ⁻¹]	7.2×10^{-16}
k_p [m ² s ⁻¹]	1.0×10^{-19}
$N_{Si}^{(1)}$	1.7×10^{-4}
$N_{Si}^{(2)}$	4.8×10^{-3}

much longer exposure times are needed to grow reasonably thick and measurable layers [35]. Therefore, k_p for SiO₂ grown in an austenitic steel at 900 °C was taken from [87] which was in very good agreement with the value from similar studies [88]. The kinetic parameters are summarized in Table 3 along with the calculated values of $N_{Si}^{(1)}$ and $N_{Si}^{(2)}$.

Given the fact that Wagner's model was originally developed to evaluate the stability of external scales in binary alloys as well as uncertainties of some kinetic parameters such as k_p in Table 3, the predicted critical silicon contents should be viewed only as approximate estimates. Nevertheless, the predicted $N_{Si}^{(1)}$ and $N_{Si}^{(2)}$ values successfully explain the difference between AM and CM oxidation morphologies.

Both CM and AM alloys are predicted to form a SiO₂ subscale as the Si content in both alloys exceeds the value $N_{Si}^{(1)} = 1.7 \times 10^{-4}$ (0.009 wt%). This finding is not surprising as the oxygen permeability $N_O^{(S)}D_O$ is extremely low underneath Cr₂O₃. However, only CM alloy 625 containing 0.28 wt% Si can maintain the SiO₂ scaling while the second Wagnerian criterion requires at least 0.24 wt% ($N_{Si}^{(2)} = 4.8 \times 10^{-3}$) to be present in the alloy. Clearly, AM is incapable of sustaining the SiO₂ subscale and therefore shows no characteristic enrichment-depletion pattern of the subsurface Si-concentration profiles (Fig. 7b).

In the diffusion modeling above, silicon is quantitatively shown to play a key role in suppressing intergranular oxidation attack in NiCr-base alloys such as 625 and 718 during high-temperature corrosion. It is evident that the AM technology for a number of reasons, e.g., powder manufacturing routes, weldability, oxidation during printing, may require minor variations of the alloy chemical composition, albeit within the specification. These modifications may in turn have serious consequences for e.g. oxidation resistance of an AM high-temperature alloy as demonstrated in the present study for alloy 625. Fine-tuning of the chemical composition to obtain the optimum mechanical as well as chemical properties of AM Ni-base superalloys thus becomes one of the numerous challenges to be addressed by the AM technology in the future.

5. Conclusions

1. Additively manufactured (AM) alloy 625 is prone to intergranular oxidation attack demonstrating a characteristic oxide scale morphology: oxide ridges over grain boundaries (GBs) accompanied by void formation along the underlying GBs, which eventually oxidize. The latter behavior is not common for conventionally manufactured (CM), e.g. hot-forged alloy 625.
2. Analysis of minor variations in chemical composition between AM and CM revealed the key role of Si in intergranular oxidation of alloy 625. Diffusion analysis confirmed the inability of AM alloy 625, containing only 0.08 wt% of Si, to sustain the SiO₂ sublayer growth while CM alloy 625 is sufficiently alloyed with Si to form and maintain the SiO₂ scale.
3. Experiments with model alloys confirmed the Si hypotheses: while Si-free alloy suffered from intergranular oxidation, alloying with Si completely eliminated oxide buckling as well as oxidation of GB

voids. Additionally, formation of a SiO₂ subscale decrease the scaling rate of Cr₂O₃ and its adhesion.

4. The SiO₂ sublayer is believed to block the excessive Cr transport at GBs leading to formation of oxide ridges over GBs, elongated voids below them and their eventual oxidation.

CRedit authorship contribution statement

Anton Chyrkin: Conceptualization, Investigation, Writing – original draft, Writing – review & editing, **Wojciech J. Nowak:** Investigation, **Kerem O. Gunduz:** Investigation, Writing – original draft, Writing – review & editing, **Irina Fedorova:** Investigation, **Mohammad Sattari:** Investigation, **Mats Halvarsson:** Writing – review & editing, Funding acquisition, Project administration, **Jan Froitzheim:** Writing – review & editing, Funding acquisition, Project administration, **Krystyna Stiller:** Writing – original draft, Writing – review & editing. All authors reviewed the results and approved the final version of the manuscript.

Declaration of Competing Interest

The authors declare that they have no known competing financial interests or personal relationships that could have appeared to influence the work reported in this paper.

Data Availability

The raw/processed data required to reproduce these findings will be made available on request.

Acknowledgements

This study was accomplished within the Swedish High Temperature Corrosion Centre (HTC) partly funded by the Swedish Energy Agency and its member companies (in this work Siemens Energy AB, AB Sandvik Materials Technology, Kanthal AB). The authors also gratefully acknowledge Chalmers Materials Analysis Laboratory (CMAL) where the materials characterizations were carried out. Dr. D. Naumenko from Forschungszentrum Jülich GmbH, Jülich, Germany is kindly acknowledged for providing CM alloy 625. Anton Chyrkin acknowledges funding from the Swedish Strategic Foundation SSF, grant No. UKR22-0047. All persons who have made substantial contributions to the work reported in the manuscript (e.g., technical help, writing and editing assistance, general support), but who do not meet the criteria for authorship, are named in the Acknowledgements and have given us their written permission to be named. If we have not included an Acknowledgements, then that indicates that we have not received substantial contributions from non-authors.

References

- [1] S. Sanchez, P. Smith, Z. Xu, et al., Powder bed fusion of nickel-based superalloys: a review, *Int. J. Mach. Tools Manuf.* 165 (2021), 103729.
- [2] T.M. Pollock, S. Tin, Nickel-based superalloys for advanced turbine engines: chemistry, microstructure and properties, *J. Propuls. Power* 22 (2006) 361–374.
- [3] I. Yadroitsev, I. Shishkovsky, P. Bertrand, I. Smirnov, Manufacturing of fine-structured 3D porous filter elements by selective laser melting, *Appl. Surf. Sci.* 255 (2009) 5523–5527.
- [4] Gebisa A.W., Lemu H.G. Additive Manufacturing for the Manufacture of Gas Turbine Engine Components: Literature Review and Future Perspectives. ASME Turbo Expo 2018: Turbomachinery Technical Conference and Exposition. 2018; doi:10.1115/GT2018-76686.
- [5] D. Monceau, M. Vilasi, High temperature oxidation of additively manufactured structural alloys, *JOM* 74 (2022) 1659–1667.
- [6] C. Juillet, A. Oudriss, J. Balmain, X. Feaugas, F. Pedraza, Characterization and oxidation resistance of additive manufactured and forged IN718 Ni-based superalloys, *Corros. Sci.* 142 (2018) 266–276.
- [7] T. Sanvienvongsa, D. Monceau, B. Macquaire, High temperature oxidation of IN 718 manufactured by laser beam melting and electron beam melting: effect of surface topography, *Corros. Sci.* 141 (2018) 127–145.

- [8] T. Sanvievongsa, D. Monceau, C. Desgranges, B. Macquaire, Intergranular oxidation of Ni-base alloy 718 with a focus on additive manufacturing, *Corros. Sci.* 170 (2020), 108684.
- [9] C. Hong, D. Gu, D. Dai, et al., High-temperature oxidation performance and its mechanism of TiC/Inconel 625 composites prepared by laser metal deposition additive manufacturing, *J. Laser Appl.* 27 (2015) S17005.
- [10] N. Ramenatte, A. Vernouillet, S. Mathieu, A. Vande Put, M. Vilasi, D. Monceau, A comparison of the high-temperature oxidation behaviour of conventional wrought and laser beam melted Inconel 625, *Corros. Sci.* (2020) 164.
- [11] M.R. Condruz, G. Matache, A. Paraschiv, T. Badea, V. Badilă, High temperature oxidation behavior of selective laser melting manufactured IN 625, *Metals* 10 (2020) 668.
- [12] E.R. Lewis, M.P. Taylor, B. Attard, et al., Microstructural characterisation and high-temperature oxidation of laser powder bed fusion processed Inconel 625, *Mater. Lett.* 311 (2022), 131582.
- [13] S. Parizia, G. Marchese, M. Rashidi, et al., Effect of heat treatment on microstructure and oxidation properties of Inconel 625 processed by LPBF, *J. Alloy. Compd.* 846 (2020), 156418.
- [14] G. de Leon Nope, G. Wang, J.M. Alvarado-Orozco, B. Gleeson, Role of elemental segregation on the oxidation behavior of additively manufactured alloy 625, *JOM* 74 (2022) 1698–1706.
- [15] K. Kunze, T. Etter, J. Grässlin, V. Shklover, Texture, anisotropy in microstructure and mechanical properties of IN738LC alloy processed by selective laser melting (SLM), *Mater. Sci. Eng. A* 620 (2015) 213–222.
- [16] A. Rezaei, A. Rezaeian, A. Kermanpur, et al., Microstructural and mechanical anisotropy of selective laser melted IN718 superalloy at room and high temperatures using small punch test, *Mater. Charact.* 162 (2020), 110200.
- [17] C. Pleass, S. Jothi, Influence of powder characteristics and additive manufacturing process parameters on the microstructure and mechanical behaviour of Inconel 625 fabricated by Selective Laser Melting, *Addit. Manuf.* 24 (2018) 419–431.
- [18] H. Helmer, A. Bauereiß, R.F. Singer, C. Körner, Grain structure evolution in Inconel 718 during selective electron beam melting, *Mater. Sci. Eng. A* 668 (2016) 180–187.
- [19] G. Marchese, S. Parizia, M. Rashidi, et al., The role of texturing and microstructure evolution on the tensile behavior of heat-treated Inconel 625 produced via laser powder bed fusion, *Mater. Sci. Eng. A* 769 (2020), 138500.
- [20] R. Muñoz-Moreno, V.D. Divya, S.L. Driver, et al., Effect of heat treatment on the microstructure, texture and elastic anisotropy of the nickel-based superalloy CM247LC processed by selective laser melting, *Mater. Sci. Eng. A* 674 (2016) 529–539.
- [21] J. Lee, M. Terner, S. Jun, H.-U. Hong, E. Copin, P. Lours, Heat treatments design for superior high-temperature tensile properties of Alloy 625 produced by selective laser melting, *Mater. Sci. Eng. A* 790 (2020), 139720.
- [22] Y.-L. Kuo, S. Horikawa, K. Kakehi, Effects of build direction and heat treatment on creep properties of Ni-base superalloy built up by additive manufacturing, *Scr. Mater.* 129 (2017) 74–78.
- [23] L.N. Carter, X. Wang, N. Read, et al., Process optimisation of selective laser melting using energy density model for nickel based superalloys, *Mater. Sci. Technol.* 32 (2016) 657–661.
- [24] G. Marchese, G. Basile, E. Bassini, et al., Study of the microstructure and cracking mechanisms of hastelloy X produced by laser powder bed fusion, *Materials* (2018) 11.
- [25] L.L. Parimi, A.R.G. Clark, D. Attallah, M.M. Microstructural and texture development in direct laser fabricated IN718, *Mater. Charact.* 89 (2014) 102–111.
- [26] J.A. Gonzalez, J. Mireles, S.W. Stafford, M.A. Perez, C.A. Terrazas, R.B. Wicker, Characterization of Inconel 625 fabricated using powder-bed-based additive manufacturing technologies, *J. Mater. Process. Technol.* 264 (2019) 200–210.
- [27] A. Kreitberg, V. Brailovski, S. Turenne, Effect of heat treatment and hot isostatic pressing on the microstructure and mechanical properties of Inconel 625 alloy processed by laser powder bed fusion, *Mater. Sci. Eng. A* 689 (2017) 1–10.
- [28] W. Tillmann, C. Schaak, J. Nellesen, M. Schaper, M.E. Aydinöz, K.-P. Hoyer, Hot isostatic pressing of IN718 components manufactured by selective laser melting, *Addit. Manuf.* 13 (2017) 93–102.
- [29] S. Sanchez, G. Gaspard, C.J. Hyde, I.A. Ashcroft, G.A.R. Clare AT, The creep behaviour of nickel alloy 718 manufactured by laser powder bed fusion, *Mater. Des.* 204 (2021), 109647.
- [30] J. Nguejio, F. Szmytka, S. Hallais, A. Tanguy, S. Nardone, M. Godino Martinez, Comparison of microstructure features and mechanical properties for additive manufactured and wrought nickel alloys 625, *Mater. Sci. Eng. A* 764 (2019), 138214.
- [31] Dryepondt S., Kirka M.M., List III F.A. Oxidation Behavior of Ni-Based Alloys Fabricated by Additive Manufacturing. In: 2019.
- [32] Romedenne M., Stack P., Pillai R., Dryepondt S. Isothermal and Cyclic Oxidation of Haynes 282 Processed by Electron Beam Melting (EBM) and Laser Powder Bed Fusion (LPBF) in Dry Air at 800 and \$\\$950\text{--}109647. *JOM*. 2022;74:1–12.
- [33] K.Y. Pineda-Arriaga, J.H. Ramírez-Ramírez, F.A. Pérez-González, J.M. Alvarado-Orozco, R. Colás, N.F. Garza-Montes-de-Oca, Characterization of the high-temperature oxidation behavior of inconel 625® fabricated by additive manufacturing and conventional methods, *Oxid. Met.* 98 (2022) 489–510.
- [34] A. Chyrkin, K.O. Gunduz, I. Fedorova, et al., High-temperature oxidation behavior of additively manufactured IN625: Effect of microstructure and grain size, *Corros. Sci.* (2022) 205.
- [35] A. Chyrkin, P. Huczowski, V. Shemet, L. Singheiser, W.J. Quadakkers, Sub-scale depletion and enrichment processes during high temperature oxidation of the nickel base alloy 625 in the temperature range 900–1000 °C, *Oxid. Met.* (2011) 75.
- [36] P. Huczowski, W. Lehnert, H.-H. Angermann, et al., Effect of gas flow rate on oxidation behaviour of alloy 625 in wet air in the temperature range 900–1000 °C, *Mater. Corros.* (2017) 68.
- [37] L. García-Fresnillo, A. Chyrkin, C. Böhme, J. Barnikel, F. Schmitz, W. J. Quadakkers, Oxidation behaviour and microstructural stability of alloy 625 during long-term exposure in steam, *J. Mater. Sci.* (2014) 49.
- [38] H. Buscail, R. Rolland, C. Issartel, et al., Effects of water vapour on the oxidation of a nickel-base 625 alloy between 900 and 1,100 °C, *J. Mater. Sci.* 46 (2011) 5903–5915.
- [39] D.J. Young, Effects of water vapour on the oxidation of chromia formers, *Mater. Sci. Forum* 595–598 (2008) 1189–1197.
- [40] A. Galerie, J.P. Petit, Y. Wouters, J. Mougin, A. Srirual, P.Y. Hou, Water vapour effects on the oxidation of chromia-forming alloys, *Mater. Sci. Forum* 696 (2011) 200–205.
- [41] J.-P. Pfeifer, H. Holzbrecher, W.J. Quadakkers, U. Breuer, W. Speier, Quantitative analysis of oxide films on ODS-alloys using MCs+-SIMS and e-beam SNMS, *Fr. J. Anal. Chem.* 346 (1993) 186–191.
- [42] W.J. Quadakkers, A. Elschner, W. Speier, H. Nickel, Composition and growth mechanisms of alumina scales on FeCrAl-based alloys determined by SNMS, *Appl. Surf. Sci.* 52 (1991) 271–287.
- [43] W.J. Nowak, Characterization of oxidized Ni-based superalloys by GD-OES, *J. Anal. Spectrom.* 32 (2017) 1730–1738.
- [44] A. Galerie, F. Toscan, M. Dupeux, et al., Stress and adhesion of chromia-rich scales on ferritic stainless steels in relation with spallation, *Mater. Res.* 7 (2004) 81–88.
- [45] A. Chyrkin, K.O. Gunduz, I. Fedorova, et al., High-temperature oxidation behavior of additively manufactured IN625: effect of microstructure and grain size, *Corros. Sci.* (2022) (accepted).
- [46] M. Calandri, D. Manfredi, F. Calignano, et al., Solution treatment study of inconel 718 produced by SLM additive technique in view of the oxidation resistance, *Adv. Eng. Mater.* 20 (2018) 1800351.
- [47] M. Liu, W. Zheng, J. Xiang, Z. Song, E. Pu, H. Feng, Grain growth behavior of inconel 625 superalloy, *J. Iron Steel Res. Int.* 23 (2016) 1111–1118.
- [48] A. Taylor, K. Sachs, A new complex eta-carbide, *Nature* 169 (1952), 411–411.
- [49] A. Chyrkin, R. Pillai, H. Ackermann, et al., Modeling carbide dissolution in alloy 602 CA during high temperature oxidation, *Corros. Sci.* (2015) 96.
- [50] R. Pillai, H. Ackermann, H. Hattendorf, S. Richter, Evolution of carbides and chromium depletion profiles during oxidation of alloy 602 CA, *Corros. Sci.* 75 (2013) 28–37.
- [51] A. Jalowicka, R. Duan, P. Huczowski, et al., Effect of specimen thickness on microstructural changes during oxidation of the NiCrW alloy 230 at 950–1050 °C, *JOM* (2015) 67.
- [52] G.A. Davies, A.B. Ponter, I.A. Menzies, Effect of interstitial atoms on a lattice-vacancy diffusional process, *Nature* 209 (1966) 1125–1126.
- [53] S.V. Divinski, G. Reglitz, G. Wilde, Grain boundary self-diffusion in polycrystalline nickel of different purity levels, *Acta Mater.* 58 (2010) 386–395.
- [54] O.A. Lukianova, V. Kulitckii, Z. Rao, Z. Li, G. Wilde, S.V. Divinski, Self-diffusion in carbon-alloyed CoCrFeMnNi high entropy alloys, *Acta Mater.* 237 (2022), 118136.
- [55] S. Cruchley, H.E. Evans, M.P. Taylor, M.C. Hardy, S. Stekovic, Chromia layer growth on a Ni-based superalloy: Sub-parabolic kinetics and the role of titanium, *Corros. Sci.* 75 (2013) 58–66.
- [56] Y. Inoue, N. Hiraide, A. Hayashi, K. Ushioda, Effect of titanium on oxidation behavior of high-purity ferritic stainless steel, *Mater. Trans.* 60 (2019) 1968–1976.
- [57] P. Berthod, F. Allègre, E. Kretz, Influence of titanium on the high temperature oxidation and chromia volatilization of ternary Ni–Cr–C alloys, *Oxid. Met.* 86 (2016) 581–595.
- [58] S. Pedrazzini, D.J. Child, G. West, et al., Oxidation behaviour of a next generation polycrystalline Mn containing Ni-based superalloy, *Scr. Mater.* 113 (2016) 51–54.
- [59] G.R. Holcomb, D.E. Alman, The effect of manganese additions on the reactive evaporation of chromium in Ni-Cr alloys, *Scr. Mater.* 54 (2006) 1821–1825.
- [60] V. Miguel-Pérez, A. Martínez-Amesti, M.L. Núñez, A. Larrañaga, M.I. Arriortua, Oxide scale formation on different metallic interconnects for solid oxide fuel cells, *Corros. Sci.* 60 (2012) 38–49.
- [61] D.W. Yun, S.M. Seo, H.W. Jeong, Y.S. Yoo, The effects of the minor alloying elements Al, Si and Mn on the cyclic oxidation of Ni–Cr–W–Mo alloys, *Corros. Sci.* 83 (2014) 176–188.
- [62] B. Hua, Y. Kong, W. Zhang, J. Pu, B. Chi, L. Jian, The effect of Mn on the oxidation behavior and electrical conductivity of Fe–17Cr alloys in solid oxide fuel cell cathode atmosphere, *J. Power Sources* 196 (2011) 7627–7638.
- [63] M. Stanislowski, J. Frotzheim, L. Niewolak, et al., Reduction of chromium vaporization from SOFC interconnectors by highly effective coatings, *J. Power Sources* 164 (2007) 578–589.
- [64] J. Frotzheim, G.H. Meier, L. Niewolak, et al., Development of high strength ferritic steel for interconnect application in SOFCs, *J. Power Sources* 178 (2008) 163–173.
- [65] A. Chyrkin, W.G. Sloof, R. Pillai, et al., Modelling compositional changes in nickel base alloy 602 CA during high temperature oxidation, *Mater. High. Temp.* (2015) 32.
- [66] H. Hindam, D.P. Whittle, High temperature internal oxidation behaviour of dilute Ni-Al alloys, *J. Mater. Sci.* 18 (1983) 1389–1404.
- [67] D.L. Douglass, J.S. Armijo, The effect of silicon and manganese on the oxidation mechanism of Ni–20 Cr, *Oxid. Met.* 2 (1970) 207–231.
- [68] J. Truman, K. Pirt, The influence of the content of certain incidental elements on the cyclic oxidation resistance of 12–13% chromium steels, *Corros. Sci.* 16 (1976) 103–108.
- [69] H.E. Evans, D.A. Hilton, R.A. Holm, S.J. Webster, Influence of silicon additions on the oxidation resistance of a stainless steel, *Oxid. Met.* 19 (1983) 1–18.

- [70] R.C. Lobb, J.A. Sasse, H.E. Evans, Dependence of oxidation behaviour on silicon content of 20%Cr austenitic steels, *Mater. Sci. Technol.* 5 (1989) 828–834.
- [71] F.H. Stott, G.J. Gabriel, G.C. Wood, The influence of silicon on the high-temperature oxidation of nickel, *Oxid. Met.* 28 (1987) 329–345.
- [72] F.H. Stott, F.I. Wei, Comparison of the effects of small additions of silicon or aluminum on the oxidation of iron-chromium alloys, *Oxid. Met.* 31 (1989) 369–391.
- [73] J. Robertson, M.I. Manning, Healing layer formation in Fe–Cr–Si ferritic steels, *Mater. Sci. Technol.* 5 (1989) 741–753.
- [74] G. Bamba, Y. Wouters, A. Galerie, F. Charlot, A. Dellali, Thermal oxidation kinetics and oxide scale adhesion of Fe–15Cr alloys as a function of their silicon content, *Acta Mater.* 54 (2006) 3917–3922.
- [75] B. Li, B. Gleeson, Effects of silicon on the oxidation behavior of Ni-base chromia-forming alloys, *Oxid. Met.* 65 (2006) 101–122.
- [76] B. Ahmad, P. Fox, STEM analysis of the transient oxidation of a Ni-20Cr alloy at high temperature, *Oxid. Met.* 52 (1999) 113–138.
- [77] B. Gleeson, M.A. Harper, The long-term, cyclic-oxidation behavior of selected chromia-forming alloys, *Oxid. Met.* 49 (1998) 373–399.
- [78] T. Amano, High-temperature oxidation resistance of Al_2O_3 - and Cr_2O_3 -forming heat-resisting alloys with noble metals and rare earths, *ECS Trans.* 25 (2010) 3–19.
- [79] C. Wagner, Theoretical analysis of the diffusion processes determining the oxidation rate of alloys, *J. Electrochem. Soc.* 99 (1952) 369.
- [80] C. Wagner, Oxidation of alloys involving noble metals, *J. Electrochem. Soc.* 103 (1956) 571.
- [81] T.D. Nguyen, J. Zhang, D.J. Young, Effects of silicon on high temperature corrosion of Fe–Cr and Fe–Cr–Ni alloys in carbon dioxide, *Oxid. Met.* 81 (2014) 549–574.
- [82] Y. Xie, Y. Cai, J. Zhang, B. Gleeson, D.J. Young, Effects of sulphate deposits on corrosion behaviour of Ni-base alloys in wet CO_2 gas at 750 °C, *Corros. Sci.* 181 (2021), 109227.
- [83] R. Rapp, The transition from internal to external oxidation and the formation of interruption bands in silver-indium alloys, *Acta Met.* 9 (1961) 730–741.
- [84] R.A. Swalin, A. Martin, R. Olson, Diffusion of magnesium, silicon, and molybdenum in nickel, *JOM* 9 (1957) 936–939.
- [85] Barin I., Sauert F., Schultze-Rhonhof E., Sheng W.S. Thermochemical Data of Pure Substances, Part 1, Ag-Kr. VCH; 1993.
- [86] J.W. Park, C.J. Altstetter, The diffusion and solubility of oxygen in solid nickel, *Metall. Trans. A* 18 (1987) 43–50.
- [87] H.E. Evans, A.T. Donaldson, Silicon and chromium depletion during the long-term oxidation of thin-sectioned austenitic steel, *Oxid. Met.* 50 (1998) 457–475.
- [88] R. Bauer, M. Baccalaro, L.P.H. Jeurgens, M. Pohl, E.J. Mittemeijer, Oxidation behavior of Fe–25Cr–20Ni–2.8Si during isothermal oxidation at 1,286 K; life-time prediction, *Oxid. Met.* 69 (2008) 265–285.